PNAS RESEARCH ARTICLE | APPLIED PHYSICAL SCIENCES

Ginkgo seed shell provides a unique model for bioinspired design

Yuanyuan Zhang[a,b,1], Jiajun Mao[a,1], Jingsong Peng[a,1], Antoni P. Tomsia[a], Lei Jiang[a,c], and Qunfeng Cheng[a,d,2]

Edited by David Weitz, Harvard University, Cambridge, MA; received July 4, 2022; accepted October 26, 2022

Natural structural materials typically feature complex hierarchical anisotropic architectures, resulting in excellent damage tolerance. Such highly anisotropic structures, however, also provide an easy path for crack propagation, often leading to catastrophic fracture as evidenced, for example, by wood splitting. Here, we describe the weakly anisotropic structure of *Ginkgo biloba* (ginkgo) seed shell, which has excellent crack resistance in different directions. Ginkgo seed shell is composed of tightly packed polygonal sclereids with cell walls in which the cellulose microfibrils are oriented in a helicoidal pattern. We found that the sclereids contain distinct pits, special fine tubes like a "screw fastener," that interlock the helicoidal cell walls together. As a result, ginkgo seed shell demonstrates crack resistance in all directions, exhibiting specific fracture toughness that can rival other highly anisotropic natural materials, such as wood, bone, insect cuticle, and nacre. In situ characterization reveals ginkgo's unique toughening mechanism: pit-guided crack propagation. This mechanism forces the crack to depart from the weak compound middle lamella and enter into the sclereid, where the helicoidal cell wall significantly inhibits crack growth by the cleavage and breakage of the fibril-based cell walls. Ginkgo's toughening mechanism could provide guidelines for a new bioinspired strategy for the design of high-performance bulk materials.

ginkgo seed shell | mechanical design | weakly anisotropic | fracture mechanism | bioinspired

Natural structural materials exhibit outstanding mechanical properties manifested by an unusual combination of strength and toughness (1–9), often called damage tolerance. The high fracture toughness of these materials arises from efficient extrinsic toughening mechanisms, with crack deflection and bridging as the mechanisms to avoid catastrophic failure. In describing the outstanding properties of natural materials, an issue not frequently mentioned in the scientific literature is the fact that they often show highly anisotropic properties: high fracture toughness but in one direction. For example, materials with uniaxial orientation, such as wood (10) and bone (11, 12), show rather poor fracture toughness for cracks advancing along the longitudinal direction, which cause catastrophic splitting fracture (11, 13). For layered materials, such as nacre, the sliding between the platelets is restricted if the direction of the advancing crack is parallel to the platelet surfaces, resulting in easier growth for cracks (14).

Wood consists of parallel tube-like tracheids in which the cellulose fibrils are embedded in a matrix of hemicellulose and lignin (15–17). In a somewhat similar manner, bone consists of hydroxyapatite mineralized collagen fibrils that assemble into lamellar osteons (4, 18). Both wood and bone are designed to resist crack growth during a "breaking" fracture, thus preventing catastrophic failure. Once cracks start to propagate perpendicular to the longitudinally aligned sclereids (or osteons), they are deflected or bridged by weak interfaces, leading to a decrease in crack-tip stress intensity. Nacre, which acts as the protective armor for mollusks, can also effectively inhibit crack penetration from the outside due to the "brick-and-mortar" architecture assembled by aragonite platelets and organic matrix (4). While the crack propagates along the direction perpendicular to the surfaces of aragonite platelets, these platelets are forced to slide with each other, leading to crack bridging and resulting in platelet "pull-out," meaning more stress is required to drive the crack to grow (19). As a result, the interfacial interactions between the platelets are disrupted, resulting in more energy dissipation. How well this mechanism works and how effective it is depend on in which direction the crack advances (14).

Here, we show that *Ginkgo biloba* (ginkgo) seed shell, the protective stony mesotesta of the seed kernel (20), demonstrates an intricate weakly anisotropic structure design. Ginkgo seed shell is composed of polygonal sclereids that bond tightly with each other. The sclereids' inner cell wall is built by cellulose microfibrils that are oriented in a manner of helicoidal arrangement. These multilayered cell walls are further interlocked by "screw fasteners," the pits, which are formed by curled layers of cell walls. Due to the weakly anisotropic structure, ginkgo seed shell shows excellent crack resistance in the four

Significance

Ginkgo biloba (ginkgo) seed shell is composed of tightly bonded polygonal sclereids with cell walls in which the cellulose microfibrils are oriented in a helicoidal pattern. The sclereids contain distinct pits, special fine tubes that act like a "screw fastener," interlocking the helicoidal cell walls together. As a result, ginkgo seed shell demonstrates crack resistance in all directions, exhibiting specific fracture toughness that can rival other highly anisotropic natural structural materials, such as insect cuticle and nacre. Ginkgo seed shell shows architecture's role in giving natural materials their often-unique properties, and provides guidelines for a new bioinspired strategy for the design of high-performance bulk materials.

Author affiliations: [a]School of Chemistry, Key Laboratory of Bio-inspired Smart Interfacial Science and Technology of Ministry of Education, Beihang University, Beijing 100191, People's Republic of China; [b]School of Chemistry and Chemical Engineering, Inner Mongolia University, Hohhot 010021, People's Republic of China; [c]Key Laboratory of Bio-inspired Materials and Interfacial Science, Technical Institute of Physics and Chemistry, Chinese Academy of Sciences, Beijing 100190, People's Republic of China; and [d]School of Materials Science and Engineering, Zhengzhou University, Zhengzhou 450001, People's Republic of China

Author contributions: L.J. and Q.C. designed research; Y.Z., J.M., and J.P. performed research; J.P. and Q.C. analyzed data; and Y.Z., J.M., A.P.T., L.J., and Q.C. wrote the paper.

The authors declare no competing interest.

This article is a PNAS Direct Submission.

[1]Y.Z., J.M., and J.P. contributed equally to this work.

[2]To whom correspondence may be addressed. Email: cheng@buaa.edu.cn.

This article contains supporting information online at https://www.pnas.org/lookup/suppl/doi:10.1073/pnas.2211458119/-/DCSupplemental.

Published November 28, 2022.

directions that were assessed, with the range of fracture toughness between 3 and 5 MPa $m^{1/2}$. The specific fracture toughness is quite comparable to some highly anisotropic natural materials, such as nacre. The excellent crack resistance of ginkgo seed shell stems from the mechanism of pit-guided crack propagation. In situ characterization reveals that the advancing crack, induced by the pit, departs the compound middle lamella (CML), where the adjacent sclereids meet with each other, and enters into a sclereid due to the interlocking effect. During the process of crack propagation, the cell walls with helicoidal cellulose microfibril alignment are cleaved or broken to induce fiber debonding, bridging, and pull-out, consuming extra loading energy to drive the growing crack. Our discovery of this toughening mechanism of weakly anisotropic natural structural materials could provide guidelines for a new bioinspired strategy for the design of high-performance bulk materials.

Results

Ginkgo seed shell functions as a protective structural material for the kernel (Fig. 1*A*). The seed shell is the aggregation of numerous polygonal sclereids with thick cell walls, which are tightly packed with each other (Fig. 1 *B*, *F*, and *J*). In order to probe the orientation of the packed sclereids, a three-dimensional (3-D) reconstruction of the sclereids was obtained using synchrotron X-ray micro-computed tomography (micro-CT), as shown in Fig. 2 (Movie S1). Based on this reconstruction, we analyzed the orientation of the packed sclereids in ginkgo seed shell in three orthogonal directions: the longitudinal (L), the tangential (T), and the radial directions (R) (Fig. 2*A*). We found that the shape of sclereids gradually varies from the inner surface to the outer surface (along the R direction) of the seed shell. Typically, the three areas can be divided as follows (Fig. 2*B*). i) The inner portion, with about 36% thickness of the whole seed shell, consists of sclereids with an average aspect ratio of 5.3 (Fig. 2 *C* and *F* and *SI Appendix*, Fig. S1 *A–C*) that are slightly aligned along the T direction. ii) The middle portion of about 55% thickness contains the irregularly packed sclereids with an average aspect ratio of 3.2 (Fig. 2 *D* and *G* and *SI Appendix*, Fig. S1 *D–F*). iii) The outer portion comprises only 9% of the seed shell thickness (Fig. 2 *E* and *H* and *SI Appendix*, Fig. S1 *G–I*). Because the sclereids in the outer portion make up little of the seed shell and are porous with an annular structure, it is reasonable to assume that this portion contributes little to resisting the loading stress. Thus, the following discussion on the sclereids focuses mainly on the inner and middle portions of the seed shell. With a low aspect ratio of only 3.2–5.3 for the sclereids in the inner and middle portion, ginkgo seed shell can be considered a weakly anisotropic material. These sclereids in gingko shells, however, are different from the 3D puzzle sclereids of pistachios (21) and walnuts (22, 23), isodiametric sclereids of pines (23), wavy sclereids of pecans (24), or fiber bundles of coconuts (25), showing elongated sclereids in the outer portion and more equiaxed sclereids in the middle and inner portions (*SI Appendix*, Fig. S2).

The cell walls in a sclereid demonstrate a concentric layered structure, where these layers are all curved around the central lumen (Fig. 1 *D*, *H,* and *L*). This is a typical sclerenchyma cell wall (26), formed by 5–7-nm diameter cellulose microfibrils helically wound around the lumen (*SI Appendix*, Fig. S3) and embedded in a matrix of lignin and hemicellulose (27). The weight fraction for cellulose, lignin, hemicellulose, and water as well as other components (such as pectin) is 42%, 16%, 17%, and 25% respectively, measured in a ginkgo seed shell under fresh condition, by a high-performance liquid chromatography (HPLC) system (28). The cell wall shows a clear periodically layered pattern by repeated helicoidal structure. To make up the helicoidal structure, the cellulose microfibrils are aligned parallel into a layer, and these layers are further stacked and rotated periodically around the normal direction (*SI Appendix*, Fig. S4). Statistically, the number of periods in the helicoidal cell wall ranges from 8 to 12 (*SI Appendix*, Fig. S5). Also, we found that the neighboring sclereids are glued by some distinct CML as shown by the red arrows (Fig. 1*H*) with a thickness of 1.70 ± 0.14 μm (*SI Appendix*, Fig. S6 *A* and *B*). It is well known that the cell wall fluorescence originates from the presence of lignin. The lignin fluorescence spectrum covers almost the entire visible light spectrum (29–31). A confocal fluorescent

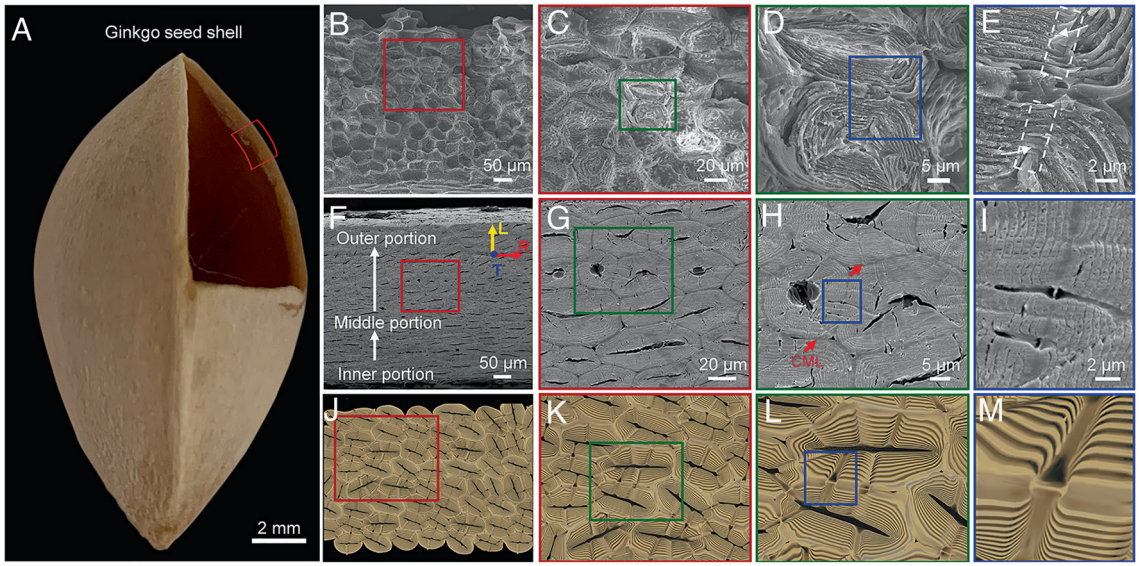

Fig. 1. Structure of the "screw fastener." (*A*) The digital image of the ginkgo seed shell. (*B–E*) SEM image of the fractured surface of the ginkgo seed shell showing the tightly packed polygonal sclereids and magnified images illustrating neighboring sclereids with interconnective pits. The dashed white areas are the pit pair and the white arrows point at the helical form of pit pairs, respectively. (*C*) Two neighboring sclereids demonstrating the concentric layered helicoidal cell wall (*D*) and pit pairs (*E*) in a symmetric and screwed form. (*F–I*) show the corresponding SEM images and (*J–M*) display a schematic illustration of the polished surface of ginkgo seed shells, interconnective sclereids, two neighboring sclereids, and pit pairs, respectively.

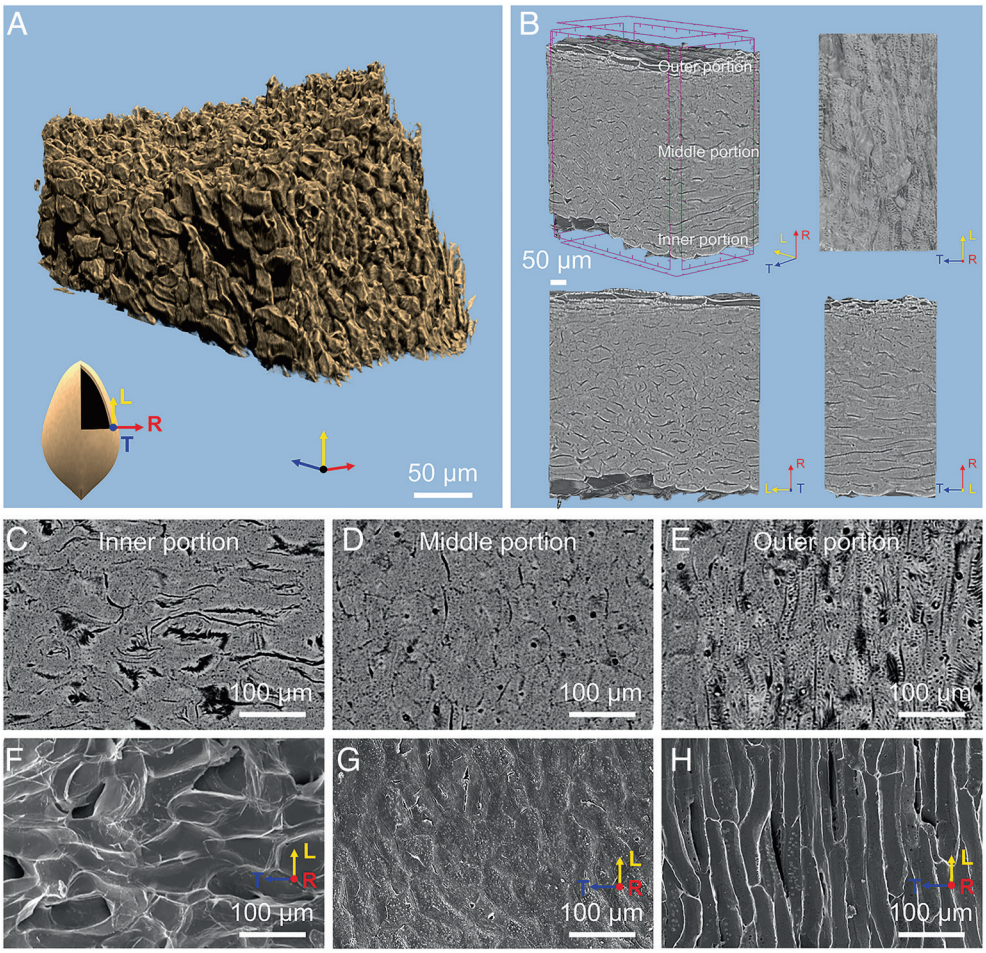

Fig. 2. X-ray micro-CT and microscopy characterization of seed shells. (*A*) 3D reconstruction of the seed shell derived from synchrotron X-ray micro-CT showing the packed sclereids. (*B*) The micro-tomography images display the three directions: longitudinal (L), tangential (T), and radial (R). (*C*–*E*) The micro-tomography images of the inner portion of the seed shell, middle portion, and the outer portion (slightly aligned along the T direction), and (*F*–*H*) the corresponding SEM images of the three areas.

microscopy image reveals that the CML exhibits stronger fluorescence, an indication of higher concentration of lignin (*SI Appendix*, Fig. S6 *C*–*F*) (30, 32, 33). This CML that is softer and weaker than the inner cell walls is shown through indentation modulus mapping (*SI Appendix*, Fig. S7) (secondary walls) (34).

Close observation of the sclereids' fracture surfaces (Fig. 1*C*) and polished cross-sections (Fig. 1*G*) shows that the neighboring sclereids contain numerous interconnective pits (Fig. 1*K*). The pits are canals that are kept free during thickening of cell walls, functioning as transport for cellular interchange of water and nutritive liquids (28, 35–37). It should be noted that some fine tubes from the cell lumen with an average diameter of 1.2 μm are just the pits (*SI Appendix*, Fig. S8), crossing two neighboring sclereids through the CML (Fig. 1 *D* and *H* and *SI Appendix*, Fig. S9). The fracture morphology of the adjacent sclereids (Fig. 1*E*) seen on polished surfaces (Fig. 1*I*), reveals that the pit is embedded in the cell wall, and the pits from the adjacent sclereids are all symmetrical with respect to the CML (Fig. 1*M*). The detailed scanning electron microscopy (SEM) images of the cross-sections of a pit pair also show that the microfibrils from two pits are oriented together at the joint (*SI Appendix*, Fig. S9), indicating that the pits are tightly connected. The pit pair structure is also visible on the SEM images obtained by ion beam milling (*SI Appendix*, Fig. S10). Lot of pits are in the ginkgo fruit, and the surface density of the pits is calculated at about 3–5 per 100 μm^2 in the middle portion and 1–3 per 100 μm^2 in the outer and inner portions according to the fracture morphology (*SI Appendix*, Fig. S11). Pits have also been found in other seed shells, such as endocarps of *Argania spinosa* (38) and *Pinus koraiensis* (23). The pit density is close to that of shells of the *A. spinosa* and *Juglans regia*, and less than that of *P. koraiensis* at 7–11 per 100 μm^2. Their location and initial shape are fixed, and during growth, the pits are rearranged by the orientation of fiber microstructure.

Our experiments show that the pit pair from the ginkgo seed shell interlocks the cell walls. The sclereids from ginkgo seed shell exhibit a multi-shelled structure (Fig. 3*A*), where the cell walls are formed by stacking layers of aligned cellulose microfibrils in a helicoidal pattern. Atomic force microscopy (AFM) images reveal the alignment of the cell walls around a pit (*SI Appendix*, Fig. S12*A*) and the helicoidal pattern of the cell wall (*SI Appendix*, Fig. S12*B*). While the seed shell is under external loading, this layered helicoidal cell wall can bear only the stress parallel to the layers effectively due to the easy tearing between the layers caused by the stress perpendicular to the layers. This pit pair structure, however, induces the curling of the helicoidal layer to form a fine tube. The cellulose microfibrils are all aligned and wound together at the edge of the pit pair as illustrated in Fig. 3 *B* and *C*, showing the orientation of the microfibrils (to simplify this schematic, the helicoidal cell wall is illustrated by microfibrils having two orthometric directions). The fracture morphology of the adjacent

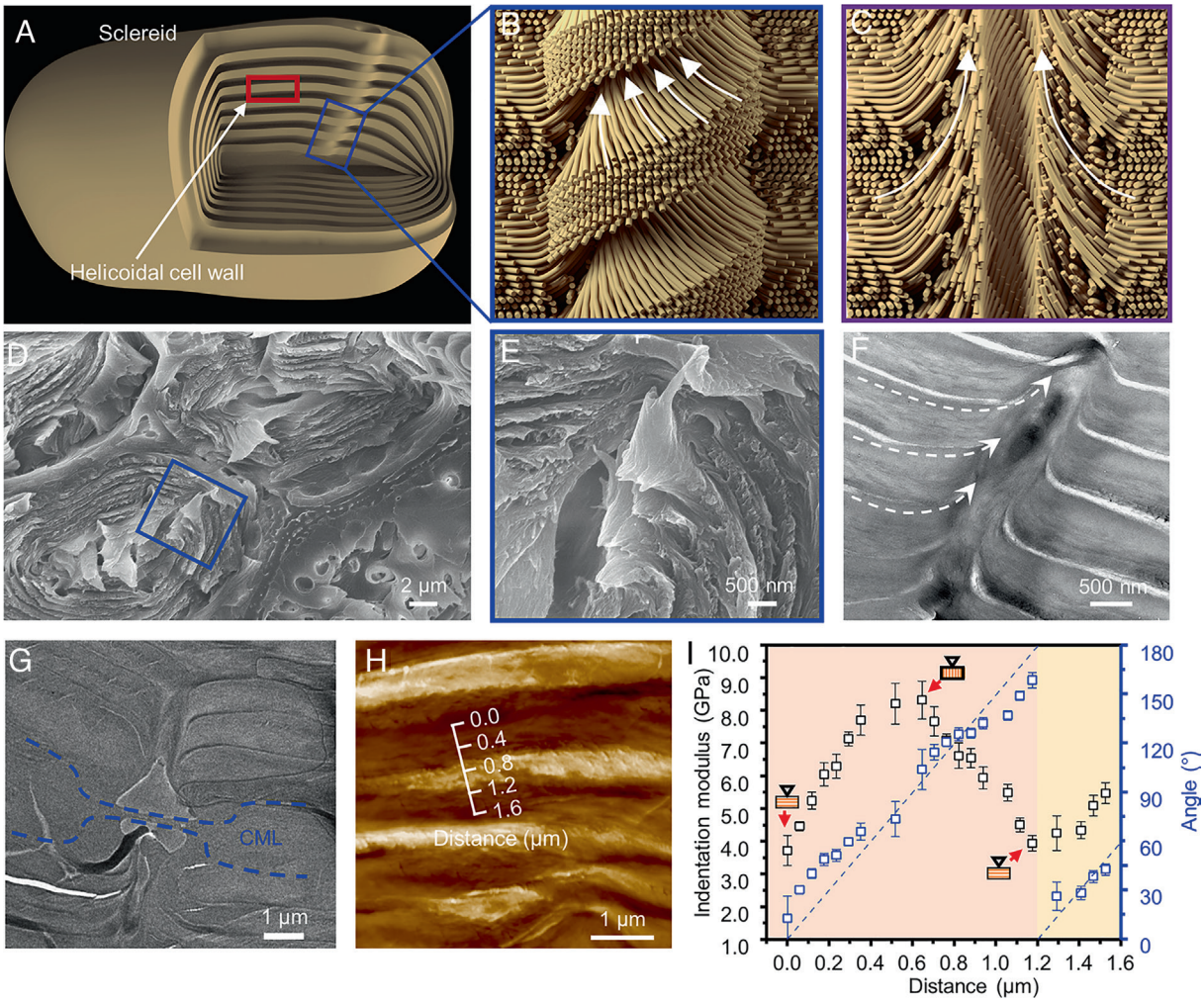

Fig. 3. Illustration of a pit pair. (*A*) Schematic illustration of a sclereid with a pit embedded in its wall. (*B*) The schematic illustration of a pit pair embedded in the cell wall and crossing the CML. The intact pit shows a helix structure like a "screw fastener" due to the microfibrils that are winding at the edge of the pit. (*C*) The schematic illustration of longitudinal section of a pit pair shows that the microfibrils are all aligned at the edge of the pit, which interlocks the layers of helicoidal cell walls. To simplify this schematic, the helicoidal structure is illustrated by microfibrils with two orthometric directions. (*D* and *E*) SEM micrographs of fracture morphology shows a pit drilling to cell walls like a "screw fastener." A higher magnification SEM image of a pit (*E*) demonstrates that the layers are curled and wound by the tubular pit. (*F*) TEM images of the longitudinal pit show that the cellulose microfibrils are all aligned along the pit and wound around the pit. (*G*) TEM image of the junction from a pit pair. The dashed blue areas are the CML. (*H*) AFM images of a cross-section of sclereids and (*I*) the influence of microfibril angles on indentation modulus as a function of distance over one pitch.

sclereids shows that the embedded pits are axially symmetrical with the CML and built by the cellulose microfibrils from the cell wall in a screwed form (Fig. 3 *D* and *E*). These cellulose microfibrils at the edge of the pit can transfer the stress between these helicoidal layers and resist the stress perpendicular to the layers, like a "screw fastener" interlocking all the helicoidal layers formed by cellulose microfibrils. The transmission electron microscopy (TEM) image of a longitudinal section of a pit (Fig. 3*F*) shows that the cellulose microfibrils are aligned along the longitudinal direction at the edge of the pit. Furthermore, in the CML a pit meets another to form a connected pit pair. The TEM image of a pit pair demonstrates that the cellulose microfibrils in a pit are aligned perpendicular to the CML where the pit is embedded (Fig. 3*G*). The helicoidal cell wall can also be verified by the measurement of indentation modulus variation probed by the AFM (39). As shown in Fig. 3 *H* and *I*, the indentation modulus changes periodically when the AFM probe is being cycled across the cell wall. Correspondingly, the angle between the cellulose fibrils as measured on the cross-section increases from 0 to 180°, indicating a helicoidal pattern. In addition, the CML can also be strengthened by a pit pair, which is embedded in it. For other natural materials, the CML is also prevalent to strengthen the interface for the improvement of resisting stress. Nacre, for example, uses mineral bridges between two adjacent aragonite nanoplatelets to resist the sliding while the strengthening takes effect at the interface only (12). However, when the adjacent sclereids in gingko seed shells are forced to separate under loading, the embedded pit pairs not only strengthen the CML, but also interlock the inner helicoidal cell wall, transferring the stress from the CML into the inside part of the sclereids, and therefore gingko seed shells resist the stress more effectively.

The weakly anisotropic structure of the ginkgo seed shell demonstrates excellent crack resistance at different locations. We conducted three-point bend testing for four crack orientations. These crack orientations are labeled by two letters using a previously reported method used for wood (10). Three orthogonal planes are the radial (R), the tangential (T), and the longitudinal or axial directions (L), respectively. The first letter illustrates the normal direction of the crack plane, while the second indicates the propagating direction. Thus, the four crack

orientations can be identified as TR, LR, LT, and TL (Fig. 4*A*). The crack orientations of RL and RT cannot be tested due to their thin thickness. As shown in Fig. 4 *B* and *C*, the fracture toughness for crack initiation (K_{IC}) in four directions shows no obvious distinction with an average value of 1.26 MPam$^{1/2}$. The K_{IC} of ginkgo seed shell is comparable to that of bone (11), illustrating good resistance for the crack initiation in four crack orientations.

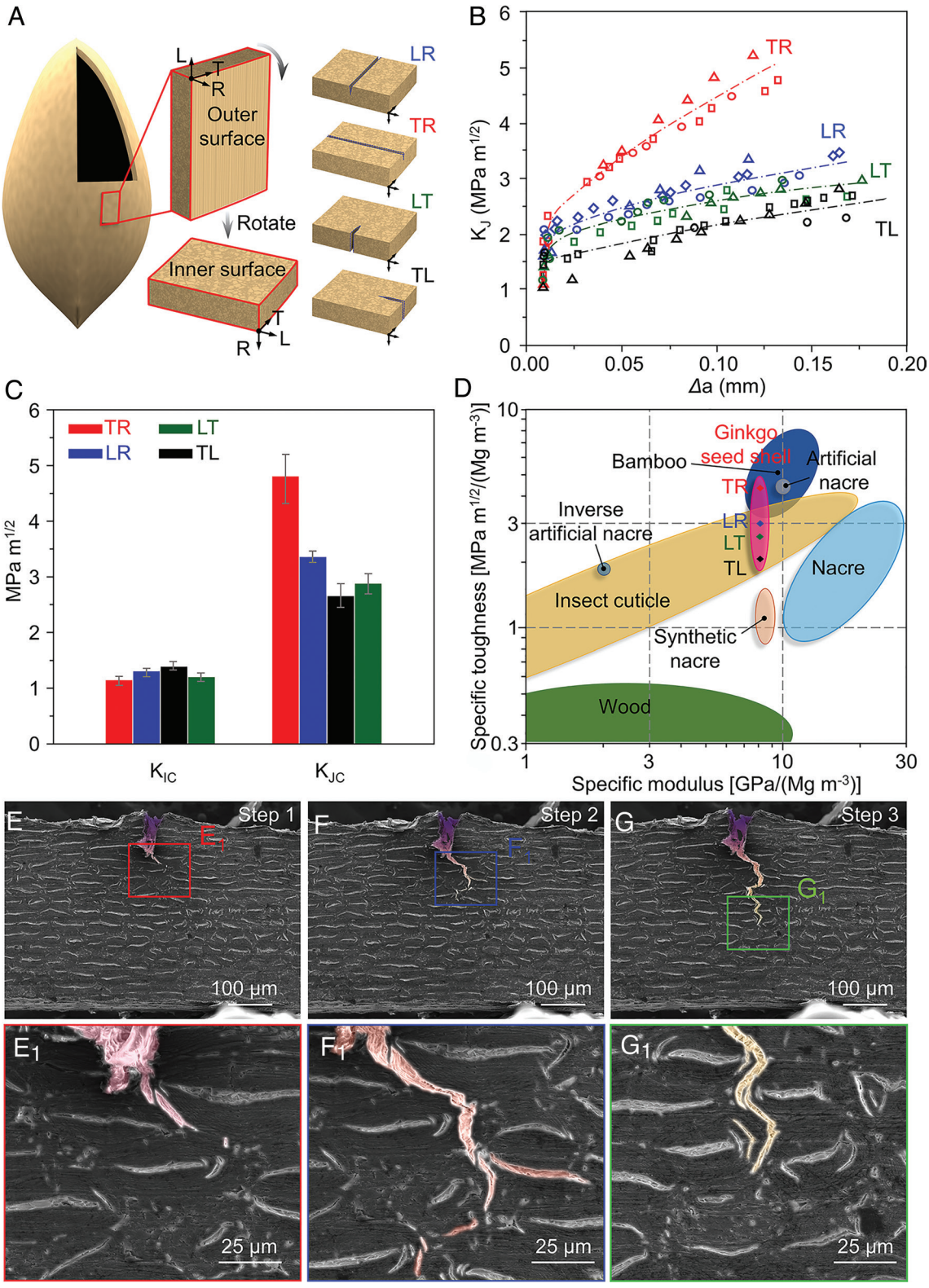

Fig. 4. Crack resistance. (*A*) Four directions of crack orientations. (*B*) The rising resistance R-curves for the cracks. (*C*) The K_{IC} and K_{JC} for the four crack orientations. (*D*) Comparison of the specific fracture toughness and specific modulus of the ginkgo seed shell in four crack orientations, along with other natural and artificial materials. (*E*–*G*) In situ fracture morphology of the single-edge notched sample with the crack orientation of LR, showing the toughening mechanism of both micro-bridging and crack deflection. (E_1–G_1) Higher magnification SEM images of the crack tips corresponding to SEM images *E*–*G*.

In addition, the rising crack-resistance curves (R-curves) for all four crack orientations demonstrate that the effective extrinsic toughening mechanism works well in all crack orientations (Fig. 4*B*), requiring more loading energy to drive the advancing crack (11, 40–47). The fracture toughness for the crack extension (K_{JC}) of the TR direction can reach up to 4.82 ± 0.37 MPa $m^{1/2}$, which is slightly higher than that of the other three crack propagation directions (3.37 ± 0.07 MPa $m^{1/2}$ for LR, 2.67 ± 0.21 MPa $m^{1/2}$ for LT, and 2.86 ± 0.17 MPa $m^{1/2}$ for TL, Fig. 4*C*). This result illustrates that the crack has more difficulty propagating along the TR direction. The anisotropy of the fracture toughness in four directions is consistent with the low but existing anisotropy in the cell orientation. However, compared with highly anisotropic natural structural materials such as bone (11) and wood (33), whose fracture toughness has more than 10-fold variation between different crack orientations, ginkgo seed shell shows weak anisotropic fracture toughness.

Discussion

The ginkgo seed shell shows unique weakly anisotropic microstructure and excellent mechanical properties among natural and artificial shell materials. To compare the ginkgo seed shell with other shell materials in more detail, we took the density into consideration and used the specific fracture toughness (K_C/ρ) and specific modulus (E/ρ) (Fig. 4*D*) determined by nanoindentation (*SI Appendix*, Fig. S13). The nanoindentation measurements were performed in the dry state with a water content of 5.64%, showing that Young's modulus of the samples decreases with increasing water content (*SI Appendix*, Table S1). In nature, protective structures and materials, such as nacre in mollusk shells (19) and exoskeletons formed by insect cuticle (46), protect fragile tissues. For the toughening mechanism, these mollusk shell and exoskeleton materials always decrease the stress around the crack tip after crack initiation through an extrinsic toughening mechanism to inhibit crack propagation, using crack deflection or bridging. Mollusk shells and exoskeletons of insects use a highly anisotropic structure to achieve more effective crack deflection and crack bridging (12, 19, 48, 49). During these processes, the abundant interfaces between the building blocks and the matrix are destroyed, thus dissipating a large amount of energy. Inspired by these mollusk shell materials, artificial shell materials, such as synthetic nacre (50), sodium alginate (SA)-based artificial nacre (51), or inverse artificial nacre (52), have been fabricated with similar highly anisotropic structures and show a significant extrinsic toughening mechanism like natural nacre (4). Under complex stress conditions, the initiation and extension of the cracks are, however, quite random. The effective fracture toughness is typically determined by the easiest mode for crack propagation (11), especially for the materials toughened by their highly anisotropic microstructure. Layered materials, such as nacre, fail if the crack advances along the direction parallel to the platelet surfaces (14). Wood is mainly composed of large aspect ratio tracheids that share cell walls with adjacent cells, and parenchyma, which is a second type of cell with radial arrangement resulting in a highly anisotropic structure (53). The failure processes of bamboo across and along its fibers also exhibit differences (54). In contrast to these anisotropic materials, the ginkgo seed shell exhibits a special weakly anisotropic structure. As shown in Fig. 4*D*, the K_C/ρ for all four directions of crack propagation are comparable to that of nacre, polymeric cellular solids (47, 55–57), insect cuticle, and other artificial shell materials (52). It is clear that the ginkgo seed shell makes full use of the extrinsic toughening mechanism based on weakly anisotropic microstructure as it shows impressive weakly anisotropic crack resistance for all four directions of crack propagation.

Similar to other natural or artificial shell materials, the ginkgo seed shell also shows a distinct extrinsic toughening mechanism: crack deflection and bridging. In situ SEM experiments were performed to reveal the mechanism of crack shielding in the ginkgo seed shell (Fig. 4 *E*–*G*). With higher magnification of the crack tip (Fig. 4 E_1–G_1), the crack deflection and branching (Fig. 4F_1), and crack bridging (Fig. 4G_1) can be clearly observed. Similar to other natural structural materials such as nacre (19), bone (11), and wood (12), the weak interfaces in the ginkgo seed shell facilitate the creation of damage tolerance. The CML between the sclereids is softer and weaker than the sclereids inside due to the higher content of lignin and pectin. The crack then tends to advance along the CML, thus generating deflection and branching. The sclereid unit can transfer deformation and induce small cracks ahead of the crack tip, thus promoting crack bridging. These mechanisms can effectively reduce the stress around the crack tip, leading to the shielding or deceleration of the crack. In the inner portion of the ginkgo seed shell, a crack in the TR direction will be more adequately deflected with a longer "zig-zag" wake (*SI Appendix*, Fig. S14), leading to more efficient crack shielding. Due to the weakly anisotropic structure, the orientation of these sclereids is difficult to distinguish. The extrinsic toughening mechanism for other crack propagation directions is also very effective.

Our experiments indicate that the unique extrinsic toughening mechanism in the ginkgo seed shell is due to the network of pits that modify the fracture behavior of the seed shell. We call this pit-guided crack propagation (Fig. 5 and *SI Appendix*, Fig. S15). By comparing the SEM images of the ginkgo seed shell before (Fig. 5 *A*–*C*) and after (Fig. 5 A_1–C_1) three-point bend testing, the pit-guided crack propagation is revealed. As shown in Fig. 5 *B* and *C*, many pits can be observed on the cross-section of the sample of three-point bend testing as shown by the white arrows. With applied loading, the prenotched crack propagates along the CML, and the helicoidal cell walls of the sclereids close to the CML generate the delamination and cleavage (Fig. 5B_1). The detailed observation of the fracture morphology reveals that the entrance, where the crack moves from the CML into the sclereid, is just the pit, as shown by the arrows in Fig. 5B_1, which is the same pit found in the original sample before bend testing (white arrow in Fig. 5*B*). In addition, we found that the crack could enter into the sclereid along the pits and tear an entire sclereid as shown by the arrows in Fig. 5C_1, which is the same pit shown by the white arrow in Fig. 5*C*. Furthermore, some of the sclereids were broken and the crack was terminated by the cell cavity and branched into other directions (Fig. 5C_1). While the crack departs the CML into the sclereids to cleave or break the sclereids, several cellulose microfibrils will be pulled out from the lignin-based matrix (Fig. 5 B_1 and C_1). We also conducted the same tests on the sample without the notch, and the crack propagates in a way similar to the prenotched sample, illustrating that the pit-guided crack propagation also works in arbitrary crack initiation (*SI Appendix*, Fig. S15). The in situ SEM characterization similarly shows that the crack enters into a sclereid guided by the pit (*SI Appendix*, Fig. S16) (Movie S2).

We also investigated the crack propagation mechanism induced by pits with finite element analysis (FEA). FEA revealed two basic forms of separation between sclereids: tensile (Fig. 5*D*) and shear mode (Fig. 5*E*). Cleavage of the cell wall (Fig. 5*F*) and breakage of sclereids (Fig. 5*G*) occur in these two modes. The FEA results indicate that the two fracture modes in crack propagation are determined by the stress state. If the stress state between the two sclereids is dominated by tensile mode, the crack deviation at pits tends to induce cleavage of the CML. If the stress state between two

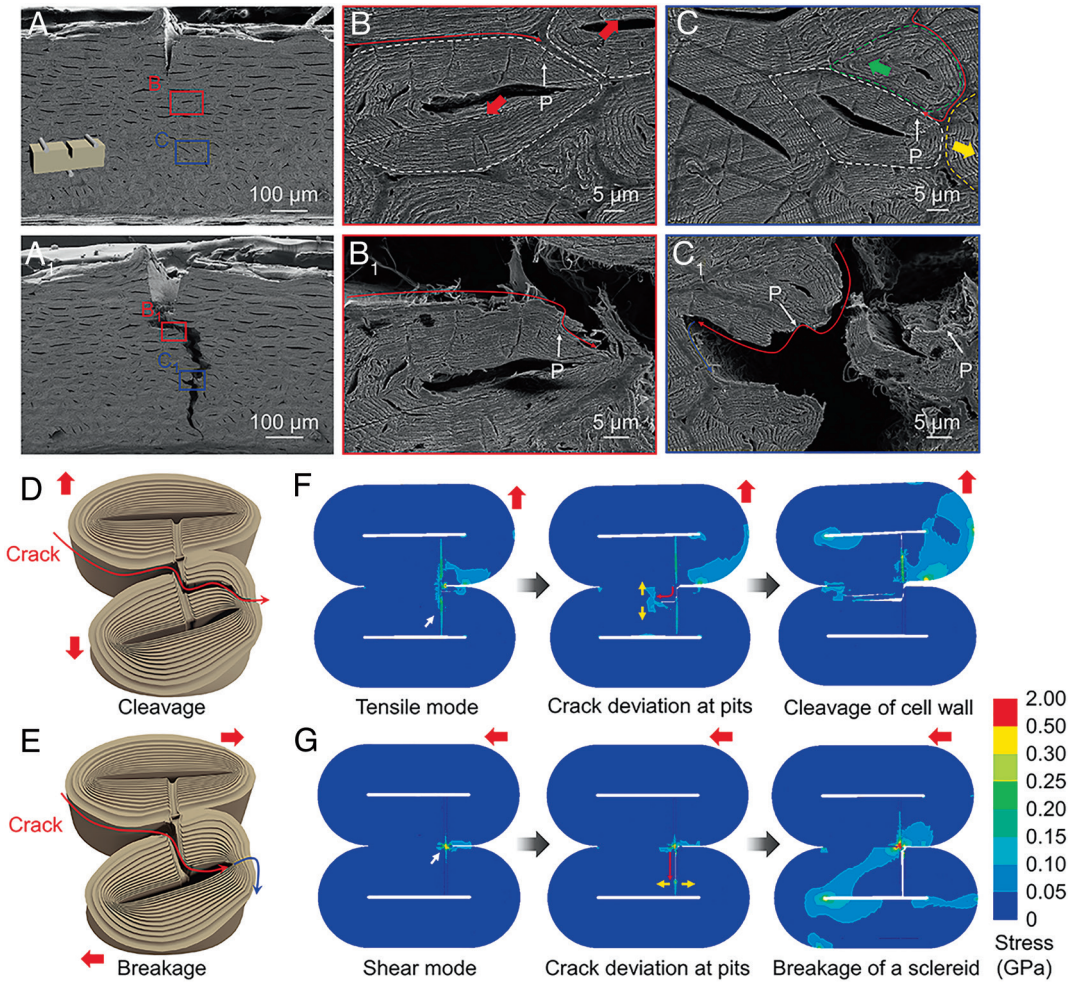

Fig. 5. Toughening mechanisms. (*A*) SEM image of a ginkgo seed shell sample before three-point bend testing. (*B* and *C*) SEM images of detailed morphologies of (*A*). (A_1) Surface morphology of a ginkgo seed shell sample after three-point bend testing. (B_1 and C_1) Higher magnification fracture morphology. The pits, shown by the white arrows, illustrate that the crack is guided into the sclereid, leading to cleavage (B_1) and breakage of the sclereid (C_1). Illustration of the proposed pit-guided crack propagation. (*D* and *E*) The pit-guided crack propagation demonstrates two possible ways of cleaving (*D*) or breaking (*E*) of a sclereid, both of which contribute to the crack shielding. (*F* and *G*) The results of FEA. (*F*) Sclereids are separated in a tensile mode, resulting in cleavage of sclereids. (*G*) Sclereids are separated in a shear mode, resulting in breakage of sclereids. "*P*" in (*B*, *C*, B_1, and C_1) represents pits.

sclereids is dominated by shear mode, the crack tends to penetrate whole cells and is terminated by the cavity, which is then deflected into another path, or continues to fracture the whole sclereids. Taking the crack propagation path shown in Fig. 5*B* as an example, the propagation (shown by the red thick arrow, Fig. 5*B*) compels the two sclereids (marked by the white dotted line) to cleave, and the cell wall is torn. Fig. 5*C* shows that the propagating crack is forcing the cell (white dotted line) into motion along the yellow arrow to the right, while the upper cell (green dotted line) is moving to the left. This results in a sliding separation between the white cell and the green cell, and the breakage of sclereids occurs.

The weak interphase between the cell structure and pit interlocking effect in the cell directs the crack path, promoting stable crack growth and increasing the fracture resistance of the seed shell. As shown in Fig. 5*D*, when the crack meets the pit, the crack originally advancing along the CML must break along cellulose orientation of the pits to propagate further. Because the pit interlocks the helicoidal cell walls, the seed shell can resist the stress at the crack tip that separates the neighboring sclereids. From the fracture morphology, a considerable part of the fracture is guided by pits (Fig. 6 *A* and *B*). The intact cell is divided into two parts when the crack meets the pits at the edge of the cells (Fig. 6 *C* and *D*). Close observation of the pits in fractured sclereids shows a break of cellulose arrangement around the pit (like the "hollow screw fastener" is divided into two halves) slowing down the crack advance (Fig. 6 *E* and *F*). The fracture morphology of the seed shell also shows that some of the "screw fastener" cellulose has been "pulled out" during the separation of the sclereids (*SI Appendix*, Fig. S17). The pit guides and contributes to the fracture extending into the cell, while the fracture along the cell edge is attributed to the destruction of the lignin bond between the cell walls. The area where the pit leads to the internal damage of the cell is denoted as A, and the area of the whole sample is denoted as S. The percentage of fracture induced by the pit (P = A/S × 100%) is 67.3 ± 8.6% based on analysis of 10 fractured samples. Due to the hollow structure of the pit, the pit will serve as a defect to guide the crack entering the inside of the sclereid from the CML. Because the pit is made up from the twisted helicoidal cell wall, this "interlocked" cell wall will transfer the stress into a larger area. This enhanced stress transfer will decrease the stress at the crack tip and furthermore generate more deformation of the helicoidal cell wall. During this guiding process, there are two possible ways that will promote the tear of a sclereid (Fig. 5*D*). In this process, if the adjacent sclereids are separated in tensile mode, the stratification and tearing of the cell wall will occur. If the adjacent

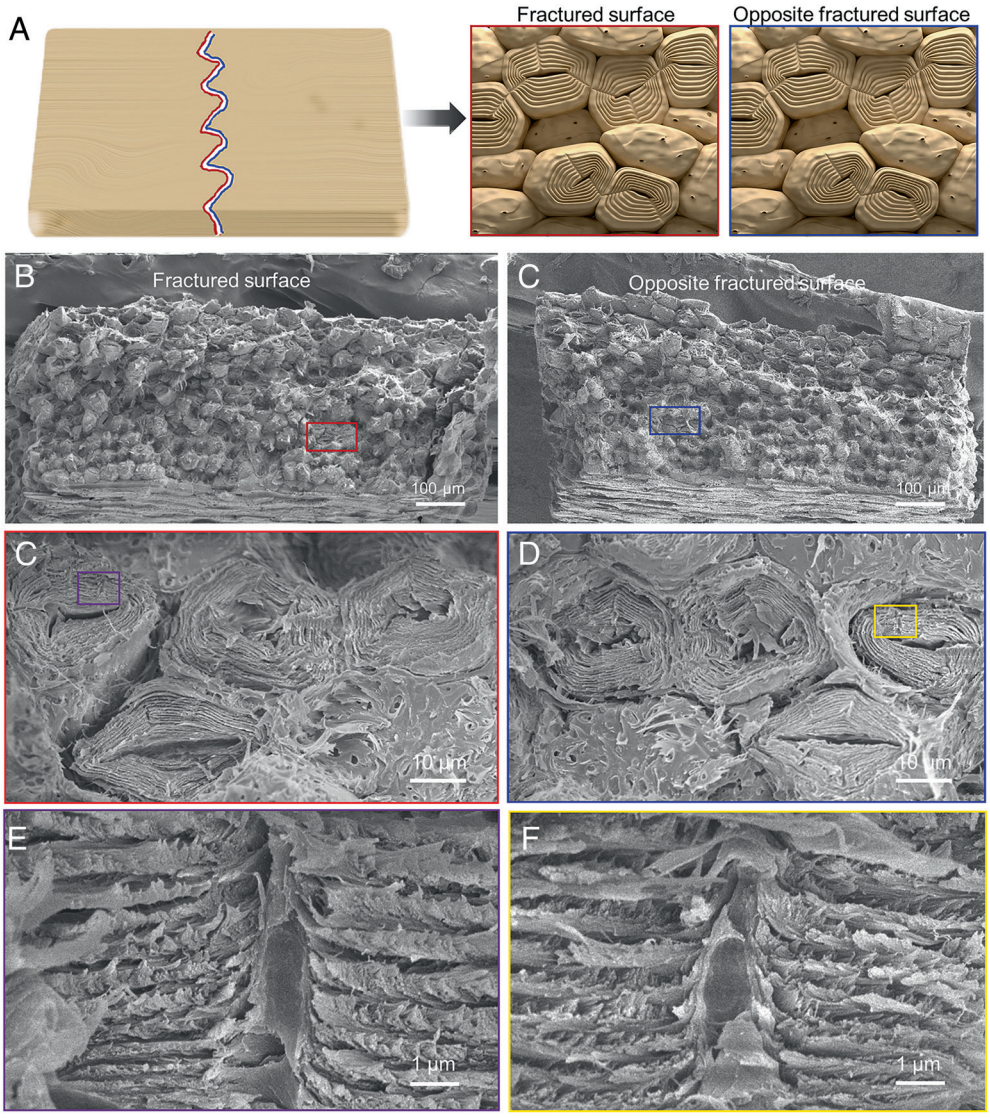

Fig. 6. SEM images of the two fractured surfaces from one sample. Schematic illustration (*A*) and SEM images of the fractured surface (*B*) and the opposite fractured surface (*C*) from a sample. SEM images of pits guiding the fracture through the cells (*C*) and left broken cells behind on the opposite fracture surface (*D*). (*E* and *F*) Enlarged view of the pits in broken cells, which shows that the break of cellulose arrangement around the pit slows the crack.

sclereids are separated by sliding, crack penetration through whole sclereids will transpire, followed by the deflection of cracks or further failure of the sclereids.

Water is the plasticizer of natural/biological materials and significantly affects their toughness (58). We compared the toughness of virgin and repeatedly hydrated and dried samples (*SI Appendix*, Fig. S18). In the virgin state, cell walls of sclereids are naturally saturated with water and contain free water in the cell lumens; the proper amount of water benefits the plasticity of the shell (53, 59). The K_{IC} value and modulus decrease as compared with the dry state, but the seed shell becomes more ductile and the final K_{JC} value is close to the dry state. After repeated hydration, the cell walls were completely filled with water. The K_{IC} and K_{JC} values were significantly reduced compared with the dry and virgin states. As shown in the stress–strain curve data for the different moisture content, the difference in toughness cannot arise from the difference in sampling direction but is instead contributed by less water content (*SI Appendix*, Fig. S19). From the fracture morphology of virgin (*SI Appendix*, Fig. S20) and repeatedly hydrated (*SI Appendix*, Fig. S21) samples, a considerable part of the fractured sclereids are guided by the pits as in the dry state. Close observation of the intact cell shows that it is divided into two parts when the crack meets the pits. The percentage of the cell fracture caused by the pits is almost the same as that in the dry state, and more moisture content did not affect the path of crack propagation induced by the pits.

During all these processes, an enormous amount of cellulose microfibrils generate fiber debonding and pull-out (Figs. 5 B_1 and C_1 and 6 *C* and *D*), similar to the toughening mechanism in bone (11), wood (10), and other fiber-reinforced nanocomposites (60). In stark contrast with bone and wood, however, the ginkgo seed shell does not use an anisotropic structure to make the crack propagate perpendicularly to the fiber orientation. For example, in other seed shells (61–64), the fracture of these shells (such as pine, Macadamia, and Brazil nuts) often occurs along the interphase of the cells, while the walnut shells tend to show fractures across the lobes of their interlocked sclereid cells, and the walnut shells show higher ultimate tensile strength (21). 3D puzzle cells of walnut shells with lobes guide the crack propagation through cells. The toughness value of pistachio is larger than that of walnut because more lobes with ball-joint-like connections are revealed in pistachio, suggesting stronger topological interlocking (21). Pits in

ginkgo shells have a similar function as lobes of 3D puzzle cells in walnuts and pistachios, extending cracks into cells. The mechanisms described above and the microstructure and high toughness of these cellulose-based materials are intriguing, and could serve as guidelines for better synthetic materials. They could provide an inspiration to seek breakthroughs in developing novel structural materials using nature's guidelines. These guidelines can also provide us with the scientific principles that could help us develop stronger and tougher structures. The germination of the ginkgo shell is different from that of walnut (23); there is a hole at one end of the shell for the seed to uptake moisture (*SI Appendix*, Fig. S22). This tiny hole has almost no effect on the fracture performance of the entire shell. A key to nature's success at making materials is that the structural architectures deployed for any one type of material may have varying lengths-of-scale that range from nanometers to micrometers. Human engineering has not been able to replicate these length-scale variances. One way to design new bionic materials would be a multiunit assembly of internal pit pair connections. We could first form helicoidal microparticles with canals by self-assembly of cellulose nanocrystals inside a tailor-made droplet (65) and then tightly pack these units together, or directly obtain them using 3D-printing technology.

Conclusion

In summary, we discovered that the ginkgo seed shell shows a unique hierarchical weakly anisotropic structure. The cellulose microfibrils are oriented into helicoidal cell walls "interlocked" by the embedded pit pairs. These cell walls construct polygonal sclereids, which are further packed in three dimensions to form a seed shell. This weakly anisotropic hierarchical structure confers crack resistance on the seed shell in all directions with a fracture toughness between 3 and 5 $MPam^{1/2}$, and the specific fracture toughness is also comparable to some natural materials with high anisotropy, such as nacre. The pit-guided crack propagation also demonstrates an effective toughening mechanism to generate weakly anisotropic crack resistance revealed by in situ characterization. The pits function as guidance to induce the crack propagation entering the sclereids, leading to the cleavage and breakage of helicoidal cell walls with large energy dissipation. Our findings could provide guidelines for a new bioinspired strategy for the design of high-performance bulk materials.

Materials and Methods

Materials. Fresh ginkgo nuts (*G. biloba*) were acquired from commercial sources in China. The nuts were stored in a refrigerator at 5°C with their outer skin on. The samples for morphology characterization and mechanical testing were taken from the fresh ginkgo nuts. The outer skin and the inner seed kernel were removed. The seed shell was washed, ultrasonically treated with deionized water, and then dried at room temperature for 6 h. The number of specimens used in each direction of bending tests, nanoindentation, and AFM was 20, and the number of specimens for quantitative 2D and 3D structural analysis was 50.

SEM Characterization. The seed shell samples were cut into fragments about 5 mm in size. The joint morphology of the sclereid unit and its surface morphology were obtained by observing the fractured section of the prepared seed shell samples in the side view, while the cross-section of the sclereid cell and its internal structure were obtained by observing the fractured section in the front view. In order to calculate the pitch of the helicoidal cell wall, the cross-sections of the samples were polished to eliminate the fiber pull-out caused by stress. The samples were cut into small pieces, ground with P800/1200/3000/5000 grade of SiC paper, and then polished with 1- and 0.2-μm diamond paste. Finally, the samples were sonicated in a water bath for 10 min to remove polishing debris and paste particles after each step. To observe the pit pair structure, the samples were prepared by ion polishing to expose the pit membrane and the pit channels. The cross-section of the sample was mechanically polished with a Leica polisher (EM TXP) and then ion polished with a Leica tri-ion polisher (EM TIC 3X). The samples were sputtered with platinum before SEM characterization. A S8010 (HITACHI) and Quanta 650 (FEG) were used to characterize the morphology of the ginkgo seed shell at an accelerating voltage of 5.0 kV and current of 10 μA.

TEM Characterization. The seed shell was cut into strips with a width of 1 mm, stained with osmium tetroxide, and then dehydrated in graded ethanol. Then the dehydrated samples were embedded in Spurr epoxy resin. The resin bulk was cut into ultrathin pieces of about 100-nm thick with an ultrathin slicer (Leica EM UC6) and placed on a copper net. An HT-7700 (HITACHI) was used at an accelerating voltage of 80 kV and current of 10.4 μA.

AFM Characterization. The seed shell was cut into strips with a width of 5 mm. The strips were initially delignified using an aqueous solution of 2 wt% $NaClO_2$ buffered with acetic acid at pH 4.6 for 6 h at 100°C. The treated samples were rinsed in ethanol–water (the volume ratio was 1:1) solutions to remove the remaining chemicals. Finally, the samples were freeze-dried at −56°C for 8 h using a freeze dryer (LGJ-12S). The resulting white powder was then exfoliated into crystalline cellulose microfibril through two steps: slight acid treatment and sonication-assisted exfoliation. To sulfate the cellulose fibers, dried soft as-treated seed shell powder (100 mg) was added into 64 wt% H_2SO_4 solution (40 mL) at 45°C with vigorous stirring for 1 h. The suspension was then diluted with cold ultrapure water (400 mL) to stop the hydrolysis reaction and allowed to settle overnight. Then the cloudy sediment was collected to purify using centrifugation with a speed of 10,000 rpm for 10 min. The supernatant was decanted, and the resulting thick white slurry was washed three times with water. To characterize the size and morphology of cellulose crystal, the as-treated cellulose dispersion was spin coated on silicon wafer at a speed of 1,000 rpm for 200 s. FASTSCANBIO (Bruker) was used with a resolution of 512 × 512 pixels with tapping mode at 3.0 Hz in the usual manner.

Confocal Microscopy Characterization. The seed shell was cut into slices with the thickness of about 10–15 μm by a microtome (Leica RM2245). The slices were placed on a glass slide, deionized water was added dropwise to wet the sample, and a coverslip was placed over the sample. An LSM 880 (Carl Zeiss) was used. Bright field and fluorescence imaging were used. The excitation wavelength of fluorescence imaging was 488 nm, and the emission wavelength was set to be 525 nm with an LP 505 filter. Due to the autofluorescence of lignin, no label was used to obtain the images, and the acquisition mode was maximum intensity projection. The scanning step length of the confocal microscope in the Z-axis direction was 0.5 μm.

Micro-CT Characterization. The seed shell sample was cut into fragments of 2 × 2mm. X-ray microscopy (Skyscan 2211 system, Bruker) was used (performed by Jinbo Wang at Bruker Inc.) at a resolution of 0.3 μm.

HPLC Characterization. HPLC was conducted to probe the weight fraction of various components from ginkgo seed shells. First, the sample of the fresh ginkgo seed shell was dried in an oven at 105°C for at least 24 h to a constant weight to determine the water content. Then, the dried sample was treated by two-step hydrolyzation with concentrated sulfuric acid (72 wt%) followed by dilute sulfuric acid (4 wt%). The cellulose and hemicellulose were hydrolyzed into soluble monosaccharides such as glucose, xylose, and arabinose in the hydrolysate. The acid-insoluble lignin was collected as the residues from the filtrated hydrolysate, and the content of lignin was determined by the difference between the dried weight of these residues and the ash weight obtained by an ashing process at 550°C. Finally, the filtrated hydrolysate was analyzed by an HPLC (Agilent 1200) to obtain the concentration of various monosaccharides. The content of cellulose was determined by the concentration of glucose while the hemicellulose was determined by the xylose and arabinose. The error caused by the degradation of monosaccharides during the hydrolyzation was corrected by the sugar recovery standard (SRS) containing glucose, xylose, and arabinose with known concentration. To determine the fraction of degraded monosaccharides, the SRS was processed in the same manner as the tested sample to obtain the concentration of monosaccharides after hydrolyzation and compared with the original known concentration.

Measurement of Young's Modulus. The ginkgo seed shell samples were cut into pieces of about 10 × 5 × 0.4 mm. The surface of 5 × 0.4 mm was polished with P800/1200/3000/5000 grade of SiC paper and then 1- and 0.2-μm diamond paste. The polished samples were sonicated in water for 10 min, and the debris left by the grinding and the particles of the abrasive paste removed. After drying at room temperature for 6 h, the specimens were glued onto a piece of iron (3 cm in diameter) for testing. Young's modulus was obtained at a load of 3,000 μN by static nanoindentation. The mechanical tests were performed using a nanoindenter (Triboindenter TI 900, Hysitron, USA) with a Berkovich tip of diamond. The indenter was placed at the middle part of the entire polished surface, to make the test more stable. The maximum load for single indentation reached 3,000 μN, and loading time, continuous loading time, and unloading time were all set at 5 s. The samples maintain a relatively dry state (water content of 5.64 *wt*%) before the fracture tests.

Fracture Toughness/R-Curve Measurements. Since the thickness of the shell is extremely thin and not fixed (about 400–500 μm), the calculation of fracture toughness cannot be based on the existing American Society for Testing and Materials (ASTM) standard. The standard (1) used in this paper can be applied to samples of different thicknesses. The shell samples were made into single-edge notched beams (SENB). All samples were polished with P800/1200/3000/5000 grade of SiC paper and then 1- and 0.2-μm diamond paste. After each step, the polishing debris and paste particles were removed from the samples in an ultrasonic bath of water for 10 min. The samples were then notched with a low-speed cutting machine (SYJ-160) to form an initial crack of roughly half the sample width, which was then sharpened with a razor blade to make the micronotch. The crack length (*a*) is about 0.4–0.6 of *W*. The values of *B* and *W* of all samples were accurately measured with a vernier caliper. *B* is the width of the specimen, and *W* is the thickness.

In situ testing of samples was carried out for stable crack extensions in a Quanta 650 SEM equipped with a field emission gun (FEG) using a Gatan Microtest 2 kN three-point bending stage (Gatan); images of the crack propagation were obtained simultaneously. These fracture tests in the vacuum did not lead to drying artifacts. All the samples maintain a relatively dry state (5.64 *wt*% water content) before the fracture tests. Except in the fracture tests, we have not seen any shrinkage or cracking under other structural analysis.

The Fracture Toughness of Virgin and Repeatedly Hydrated Ginkgo Seed Shells. Samples were made into SENB as dry samples and then polished. The virgin samples were stored at a humidity of 90% to reach balanced water content. Testing of samples was carried out under stable crack extensions in a TESmart electromechanical universal testing machine using a Microtest (1 kN) three-point bending stage. All the samples were tested in a humidity of 90% (20 wt% water content).

The repeatedly hydrated samples were soaked in water five times, each time for 1 h. Testing of samples was carried out under stable crack extensions in a TESmart electromechanical universal testing machine using a Microtest (1 kN) three-point bending stage. All the samples were taken out of the water and tested immediately in a humidity of 100%.

FEA. The modeling of finite element simulation is shown in *SI Appendix*, Scheme S1: considering the two adjacent sclereids with one pit pair, it is simplified into two thin slices with pit pairs. The sclereids are simplified into concentric circles with 10 rings to simulate the layered cell wall, and there are cohesive elements between the adjacent rings (shown by the dotted line). A cohesive element with special thickness is between adjacent sclereids, simulating the interfacial zone. The simulation is carried out through ANSYS 19.2. In order to simulate crack propagation, a self-compiler program with a global embedded interface element is used. The entity is divided into small elements, which are packed by cohesive force proactively. When the cohesive force reaches the upper limit, the elements will be deformed. If the element is small enough, it can be considered that the deformation path between the elements is close to the real crack propagation path. The calculation and solution process were submitted to the high-performance computing platform of Beihang University. The solid element adopts solid185, the modulus is set to 10 GPa, and Poisson's ratio is 0.3. For tensile mode, the cohesive strength cannot be simply assumed by the strength of the matrix, since lots of cellulose fibers will also be pulled out and form some bridges. Thus, taking the cellulose fibers into consideration, here we used the strength of wood to assume the cohesive strength. However, wood demonstrates a fairly high anisotropy, and the average strength of wood for both cleaving and breaking was used, which is about 50–60 MPa (10). As the density of the cell wall is almost double that of wood, we finally used the value of 100 MPa to assume the tensile cohesive strength. For the shear mode, the fibers barely form the bridges, so the cohesive strength can be set as the matrix of lignin and hemicellulose, which is about 10 MPa (12).

Data, Materials, and Software Availability. All study data are included in the article and/or *SI Appendix*.

ACKNOWLEDGMENTS. We thank Y. Cao at the National Key Laboratory of Chinese Academy of Forestry for TEM/fluorescence observation. We are grateful for the opportunity to use the High Performance Computing Platform at Beihang University for data processing. This work was supported by the National Key Research and Development Program of China (Grant No. 2021YFA0715700), the National Science Fund for Distinguished Young Scholars (Grant No. 52125302), National Natural Science Foundation of China (Grants No. 22075009, 51961130388, 21875010, 51522301, 21273017, 51103004, 51903125), Newton Advanced Fellowship (Grant No. NAF\R1\191235), Beijing Natural Science Foundation (Grant No. JQ19006), 111 Project (Grant No. B14009), China Postdoctoral Science Foundation (2018M640043, 2019T120038), and Program of Higher-level Talents of IMU (10000-21311201/007).

1. J. D. Currey, J. D. Taylor, The mechanical behaviour of some molluscan hard tissues. *J. Zool.* **173**, 395–406 (1974).
2. S. Amini *et al.*, Textured fluorapatite bonded to calcium sulphate strengthen stomatopod raptorial appendages. *Nat. Commun.* **5**, 3187 (2014).
3. S. Amini, M. Tadayon, S. Idapalapati, A. Miserez, The role of quasi-plasticity in the extreme contact damage tolerance of the stomatopod dactyl club. *Nat. Mater.* **14**, 943–950 (2015).
4. U. G. K. Wegst, H. Bai, E. Saiz, A. P. Tomsia, R. O. Ritchie, Bioinspired structural materials. *Nat. Mater.* **14**, 23–36 (2015).
5. H. Chen *et al.*, Continuous directional water transport on the peristome surface of Nepenthes alata. *Nature* **532**, 85–89 (2016).
6. V. C. Sundar, A. D. Yablon, J. L. Grazul, M. Ilan, J. Aizenberg, Fibre-optical features of a glass sponge. *Nature* **424**, 899–900 (2003).
7. B. Yeom *et al.*, Abiotic tooth enamel. *Nature* **543**, 95–98 (2017).
8. J. Aizenberg *et al.*, Skeleton of euplectella sp.: Structural hierarchy from the nanoscale to the macroscale. *Science* **309**, 275–278 (2005).
9. A. Miserez, T. Schneberk, C. Sun, F. W. Zok, J. H. Waite, The transition from stiff to compliant materials in squid beaks. *Science* **319**, 1816–1819 (2008).
10. M. F. Ashby, K. E. Easterling, R. Harrysson, S. K. Maiti, The fracture and toughness of woods. *Proc. R. Soc. Lond. Ser. A* **398**, 261–280 (1985).
11. K. J. Koester, J. W. Ager III, R. O. Ritchie, The true toughness of human cortical bone measured with realistically short cracks. *Nat. Mater.* **7**, 672–677 (2008).
12. F. Barthelat, Z. Yin, M. J. Buehler, Structure and mechanics of interfaces in biological materials. *Nat. Rev. Mater.* **1**, 16007 (2016).
13. H. Lichtenegger, A. Reiterer, S. E. Stanzl-Tschegg, P. Fratzl, Variation of cellulose microfibril angles in softwoods and hardwoods–a possible strategy of mechanical optimization. *J. Struct. Biol.* **128**, 257–269 (1999).
14. R. Z. Wang, H. B. Wen, F. Z. Cui, H. B. Zhang, H. D. Li, Observations of damage morphologies in nacre during deformation and fracture. *J. Mater. Sci.* **30**, 2299–2304 (1995).
15. M. A. Meyers, P.-Y. Chen, A.Y.-M. Lin, Y. Seki, Biological materials: Structure and mechanical properties. *Prog. Mater. Sci.* **53**, 1–206 (2008).
16. P. Fratzl, Biological materials: Structure and mechanical properties. *Curr. Opin. Colloid Interface Sci.* **8**, 32–39 (2003).
17. G. Pilate *et al.*, Lignification and tension wood. *C. R. Biol.* **327**, 889–901 (2004).
18. J. Buckwalter, M. Glimcher, R. Cooper, R. Recker, Bone biology. *J. Bone Joint Surg. Am.* **77**, 1256–1275 (1995).
19. F. Barthelat, H. D. Espinosa, An experimental investigation of deformation and fracture of nacre–mother of pearl. *Exp. Mech.* **47**, 311–324 (2007).
20. P. Ch'ng *et al.*, Some physical properties of gingko nuts and kernels. *Inter. Agrophys.* **27**, 485–489 (2013).
21. N. Xiao *et al.*, Twist and lock: Nutshell structures for high strength and energy absorption. *R. Soc. Open Sci.* **8**, 210399 (2021).
22. S. J. Antreich *et al.*, A belt for the cell: Cellulosic wall thickenings and their role in morphogenesis of the 3D puzzle cells in walnut shells. *J. Exp. Bot.* **72**, 4744–4756 (2021).
23. S. J. Antreich *et al.*, The puzzle of the walnut shell: A novel cell type with interlocked packing. *Adv. Sci.* **6**, 1900644 (2019).
24. J. C. Huss *et al.*, Topological interlocking and geometric stiffening as complementary strategies for strong plant shells. *Adv. Mater.* **32**, 2004519 (2020).
25. B. Gludovatz *et al.*, Multiscale structure and damage tolerance of coconut shells. *J. Mech. Behav. Biomed. Mater.* **76**, 76–84 (2017).
26. J. C. Huss, N. Gierlinger, Functional packaging of seeds. *New Phytol.* **230**, 2154–2163 (2021).
27. A. M. C. Emons, B. M. Mulder, How the deposition of cellulose microfibrils builds cell wall architecture. *Trends Plant Sci.* **5**, 35–40 (2000).

28. D. Reis, B. Vian, Helicoidal pattern in secondary cell walls and possible role of xylans in their construction. *C. R. Biol.* **327**, 785–790 (2004).
29. J. Song *et al.*, Processing bulk natural wood into a high-performance structural material. *Nature* **554**, 224–228 (2018).
30. L. A. Donaldson, K. Radotic, Fluorescence lifetime imaging of lignin autofluorescence in normal and compression wood. *J. Micro.* **251**, 178–187 (2013).
31. L. Donaldson *et al.*, Quantification of compression wood severity in tracheids of Pinus radiata D. Don using confocal fluorescence imaging and spectral deconvolution. *J. Struct. Biol.* **169**, 106–115 (2010).
32. L. A. Donaldson, J. P. Knox, Localization of cell wall polysaccharides in normal and compression wood of radiata pine: Relationships with lignification and microfibril orientation. *Plant Physiol.* **158**, 642–653 (2012).
33. B. Albinsson, S. Li, K. Lundquist, R. Stomberg, The origin of lignin fluorescence. *J. Mol. Struct.* **508**, 19–27 (1999).
34. A. Melelli, O. Arnould, J. Beaugrand, A. Bourmaud, The middle lamella of plant fibers used as composite reinforcement: Investigation by atomic force microscopy. *Molecules* **25**, 632 (2020).
35. P. Schüler, T. Speck, A. Bührig-Polaczek, C. Fleck, Structure-function relationships in macadamia integrifolia seed coats – fundamentals of the hierarchical microstructure. *PLoS One* **9**, e102913 (2014).
36. K. Wilson, Extension growth in primary cell walls with special reference to elodea canadensis. *Ann. Bot.* **21**, 1–11 (1957).
37. G. Setterfield, Structure and composition of plant-cell organelles in relation to growth and development. *Can. J. Plant Sci.* **39**, 469–489 (1961).
38. H. S. Sebaa, M. K. Harche, Anatomical structure and ultrastructure of the endocarp cell walls of Argania spinosa (L.) Skeels (Sapotaceae). *Micron* **67**, 100–106 (2014).
39. R. Yang *et al.*, AFM identification of beetle exocuticle: Bouligand structure and nanofiber anisotropic elastic properties. *Adv. Funct. Mater.* **27**, 1603993 (2017).
40. M. Koyama *et al.*, Bone-like crack resistance in hierarchical metastable nanolaminate steels. *Science* **355**, 1055–1057 (2017).
41. S. Deville, E. Saiz, R. K. Nalla, A. P. Tomsia, Freezing as a path to build complex composites. *Science* **311**, 515–518 (2006).
42. H. Peterlik, P. Roschger, K. Klaushofer, P. Fratzl, From brittle to ductile fracture of bone. *Nat. Mater.* **5**, 52–55 (2006).
43. J. Yan, J. J. Mecholsky Jr., K. B. Clifton, How tough is bone? Application of elastic–plastic fracture mechanics to bone. *Bone* **40**, 479–484 (2007).
44. F. Bouville *et al.*, Strong, tough and stiff bioinspired ceramics from brittle constituents. *Nat. Mater.* **13**, 508–514 (2014).
45. E. Munch *et al.*, Tough, bio-inspired hybrid materials. *Science* **322**, 1516–1520 (2008).
46. U. G. K. Wegst, M. F. Ashby, The mechanical efficiency of natural materials. *Philos. Mag.* **84**, 2167–2186 (2004).
47. P. Lucas *et al.*, The toughness of plant cell walls. *Philos. T. R. Soc. B* **348**, 363–372 (1995).
48. F. Barthelat, C.-M. Li, C. Comi, H. D. Espinosa, Mechanical properties of nacre constituents and their impact on mechanical performance. *J. Mater. Res.* **21**, 1977–1986 (2011).
49. F. Barthelat, H. Tang, P. Zavattieri, C. Li, H. Espinosa, On the mechanics of mother-of-pearl: A key feature in the material hierarchical structure. *J. Mech. Phys. Solids* **55**, 306–337 (2007).
50. L. B. Mao *et al.*, Synthetic nacre by predesigned matrix-directed mineralization. *Science* **354**, 107–110 (2016).
51. H.-L. Gao *et al.*, Mass production of bulk artificial nacre with excellent mechanical properties. *Nat. Commun.* **8**, 287 (2017).
52. Huang *et al.*, Ultra-tough inverse artificial nacre based on epoxy-graphene by freeze-casting. *Angew. Chem. Int. Ed.* **58**, 7636–7640 (2019).
53. A. Reiterer, S. Tschegg, The influence of moisture content on the mode I fracture behaviour of sprucewood. *J. Mater. Sci.* **37**, 4487–4491 (2002).
54. Y. L. An *et al.*, Three-point bending fracture behaviors of bamboo. *Adv. Mater. Res.* **261**, 464–468 (2011).
55. M. F. Ashby, L. J. Gibson, U. G. K. Wegst, R. Olive, The mechanical properties of natural materials. I. Material property charts. *Proc. R. Soc. Lond. Ser. A* **450**, 123–140 (1995).
56. M. F. Ashby, L. J. Gibson, *Cellular Solids: Structure and Properties* (Press Syndicate of the University of Cambridge, Cambridge, UK, 1997), pp. 175–231.
57. R. Ross, *Wood Handbook: Wood as an Engineering Material* (Dept. of Agriculture, Agriculture handbook, United States, 2012).
58. T. Ozyhar, S. Hering, P. Niemz, Moisture-dependent elastic and strength anisotropy of European beech wood in tension. *J. Mater. Sci.* **47**, 6141–6150 (2012).
59. N. Xiao *et al.*, From the soft to the hard: Changes in microchemistry during cell wall maturation of walnut shells. *Front. Plant Sci.* **11**, 466 (2020).
60. K. Yang *et al.*, Integrating tough Antheraea pernyi silk and strong carbon fibres for impact-critical structural composites. *Nat. Commun.* **10**, 3786 (2019).
61. C. Fleck *et al.*, Microstructural features influencing failure in Macadamia nuts. *Bioinsp. Biomim. Nan.* **1**, 67–75 (2012).
62. J. F. V. Vincent, Nuts. *MRS Proc.* **292**, 35–43 (1992).
63. M. Sonego, C. Fleck, L. A. Pessan, Hierarchical levels of organization of the Brazil nut mesocarp. *Sci. Rep.* **10**, 1–13 (2020).
64. C. Fleck *et al.*, Microstructural features influencing failure in Macadamia nuts. *Bioinspired Bioinsp. Biomim. Nan.* **1**, 67–75 (2012).
65. R. M. Parker *et al.*, Hierarchical self-assembly of cellulose nanocrystals in a confined geometry. *ACS Nano* **10**, 8443–8449 (2016).